Research Article

D. Mohanty, G. Mahanta, Haewon Byeon, S. Vignesh, S. Shaw, M. Ijaz Khan*, Dilsora Abduvalieva, Vediyappan Govindan*, Fuad A. Awwad, and Emad A. A. Ismail

# Thermo-solutal Marangoni convective Darcy-Forchheimer bio-hybrid nanofluid flow over a permeable disk with activation energy: Analysis of interfacial nanolayer thickness

https://doi.org/10.1515/phys-2023-0119
received July 11, 2023; accepted September 25, 2023

**Abstract:** The Marangoni convective phenomena have a unique impact on industries and medical tools. These phenomena are more prominent in the presence of dual nanoparticles (NPs) over base fluids such as blood that are surrounded by a thin interfacial nanolayer, an important feature to control the physical and thermal properties of the NP. In this problem, we have analysed the thermo-solutal Marangoni convective Darcy-Forchheimer flow of nanomaterials with the impact of the interfacial nanolayer. The results of the system of an exponential heat source, non-linear radiation, joule heating, and activation energy are discussed. An appropriate transition is applied to rationalise the substantially paired and nonlinear governing equations and then processed by the Galerkin finite element method (G-FEM). The impression of different governing parameters on the governing systems in conjunction with entropy and Bejan number is demonstrated through graphical and tabular form. Graphs are drawn with an evaluation of general and hybrid nanofluids (HNFs) and different nanolayer thicknesses of NPs. Activation energy and chemical reaction parameters restrict the Sherwood number, and the same is observed for the Nusselt number with an increase in the Brinkman and Eckert numbers. The thickness of the interfacial nanolayer of the NPs restricts the entropy generation of the system, while the entropy is higher for the HNF than the nanofluid. An opposite feature was observed for the Bejan number.

**Keywords:** thermo-solutal Marangoni convection, interfacial nanolayer thickness, bio-hybrid nanofluid, Darcy-Forchheimer flow, chemical reactions, activation energy

*** Corresponding author: M. Ijaz Khan,** Department of Mechanical Engineering, Lebanese American University, Beirut, Lebanon; Department of Mechanics and Engineering Science, Peking University, Beijing 100871, China; Department of Mathematics and Statistics, Riphah International University I-14, Islamabad 44000, Pakistan, e-mail: scientificresearchglobe@gmail.com
*** Corresponding author: Vediyappan Govindan,** Department of Mathematics, Hindustan Institute of Technology and Science, Chennai, India, e-mail: vedimalawi@gmail.com
**D. Mohanty, G. Mahanta:** Department of Mathematics, C. V. Raman Global University, Bhubaneswar-752054, India
**Haewon Byeon:** Department of AI Big data, Inje University, Gimhae, 50834, South Korea
**S. Vignesh:** Department of Mathematics, Vel Tech Rangarajan Dr. Sagunthala R&D Institute of Science and Technology, Avadi, India
**S. Shaw:** Department of Mathematics and Statistical Sciences, Botswana International University of Science and Technology, Private Bag 16, Palapye, Botswana
**Dilsora Abduvalieva:** Department of Philosophy in Pedagogical Sciences, Tashkent State Pedagogical University, Bunyodkor Avenue, 27, Tashkent, 100070, Uzbekistan
**Fuad A. Awwad, Emad A. A. Ismail:** Department of Quantitative analysis, College of Business Administration, King Saud University, P.O. Box 71115, Riyadh 11587, Saudi Arabia

## Nomenclature

| | |
|---|---|
| Br | Brinkman number |
| $C_f$ | drag coefficient |
| $E_1$ | activation energy |
| Ec | Eckert number |
| Fr | inertia coefficient |
| $F\left(=\frac{rC_s}{\sqrt{K_p}}\right)$ | non-uniform inertia coefficient |
| $I_1,\ I_2$ | ratio of nanolayer |
| $K^*$ | permeability of porous medium |
| $K_1$ | chemical reaction parameter |
| $K_p$ | permeability parameter |
| $k_{nf}$ | thermal conductivity of nanofluid |
| $k_f$ | thermal conductivity of base fluid |
| $k_s$ | thermal conductivity of nanoparticle |

| | |
|---|---|
| $L^*$ | diffusion parameter |
| $Q_T$ | heat generation parameter |
| $Re_r$ | local Reynolds number |
| Rd | radiation parameter |
| $r^*$ | Marangoni ratio parameter |
| Sc | Schmidt number |
| $T_w$ | surface temperature (K) |
| $T$ | fluid temperature ($K$) |
| $(u, w)$ | components of velocity with growing $(r,\ z)$ directions |
| $(\rho C_p)_{nf}$ | nanofluid capacitance of heat |
| $(\rho C_p)_f$ | effective heat capacitance of base fluid |
| $(\rho C_p)_s$ | |
| $\rho_s$ | solid density of nanoparticles |
| $\rho_f$ | density of base fluid |
| $\mu_{nf}$ | dynamic viscosity of nanofluid |
| $\mu_f$ | dynamic viscosity of base fluid |
| $\sigma_{nf}$ | electrical conductivity of nanofluid |
| $\sigma_s$ | electrical conductivity of nanoparticles |
| $\sigma_f$ | electrical conductivity of base fluid |
| $\mu_{hnf}$ | dynamic viscosity of hybrid nanofluid |
| $\rho_{hnf}$ | effective density of hybrid nanofluid |
| $(\rho c_p)_{hnf}$ | heat capacitance of hybrid nanofluid |
| $\sigma_{hnf}$ | electrical conductivity of hybrid nanofluid |
| $(\rho\beta)_{hnf}$ | thermal expansion of hybrid nanofluid |
| $\sigma^*$ | Stefan Boltzmann constant |
| $\lambda$ | porosity variable |
| $\Omega$ | dimensional constant |
| $\alpha_f$ | thermal diffusivity of the base fluid ($m^2\ s^{-1}$) |
| $\beta$ | dimensional constant |
| $\phi_1,\ \phi_2$ | original solid volume fractions |
| $\varphi_1,\ \varphi_2$ | upgraded volume fractions |
| $\theta_w$ | temperature ratio parameter |

# 1 Introduction

Marangoni convection is an important feature in different aspects of semiconductor processing, aerospace, crystal growth, *etc*. The numerical simulation of Marangoni flow over horizontal and vertical stretching sheets has been studied by different researchers [1–3]. Mahanthesh *et al.* [4] analysed the magnetohydrodynamic (MHD) flow through Marangoni convection of a nanofluid (NF) by rotating disk. Hayat *et al.* [5] inspected the mixed convection Marangoni flow of a Casson fluid. Lin *et al.* [6] analysed the MHD flow of the Marangoni boundary layer and the consequences of the magnetic field. Zhang *et al.* [7] analysed the numerical resolutions for Marangoni convection due to the effect of the temperature gradient. Sheikholeslami and Chamkha [8] looked into the features of NF on Marangoni convectional flow. Shaw *et al.* [9] and Mahanta *et al.* [10] analysed the Marangoni action flow of a Casson NF.

Most of the researchers focus on studying NFs due to their significant effects in engineering and related fields. NFs have a broad scope of application in thermal engineering and industrial activities, as they are applicable for improving thermal efficiency. Basically, the thermal conductivity and the specific heat are used to increase the local Nusselt number. Mousavi and Heris [11] discovered the accumulation of nanoparticles (NPs) that enhanced the thermal capacity. Makinde and Aziz [12] analysed the flow of NF by using convective boundary conditions. Ramya *et al.* [13] discussed MHDs and the viscous flow of NFs. Choudhury and Das [14] illustrated the MHD-free convection of viscoelastic fluid. HNFs have a vast application in the process of cooling. HNFs are a composite mixture of several metallic and non-metallic base fluids. Thermophysical properties of HNFs also have vast applications in the field of engineering. Because of its vital uses in bioengineering and medical sciences, such as minimising bleeding after surgery, researchers have recently concentrated more on bio-HNF flow. Researchers discussed several properties of hybrid NPs and HNFs [15–18] due to their huge applications in manufacturing and automotive industry. Xiong *et al.* [19] investigated the behaviour of the power law that contains the NPs and its effect on it. Abbas *et al.* [20] and Babar and Ali [21] discussed the applications and overall structure of HNFs. Ghalambaz *et al.* [22] analysed the mathematical modelling of HNFs at the stagnation point.

MHD is the magnetic field that reduces electrical flow in the moving conductive fluid and creates the force of the fluid, and it has immense utilisation in the areas of technology and commercial enterprise. Examples of MHD are nuclear reactor coolers, crystal growth, and power generators. Kumar *et al.* [23] illustrated the impact of magnetic dipole of maxwell NF flow with single and multiwalled carbon nanotubes (MWCNTs). Madhukesh *et al.* [24] investigated the magnetic impact of micropolar Casson NF influenced by Cattaneo-Christov heat flux. Javed *et al.* [25] explored the MHD axisymmetric flow of Casson fluid with heat absorption over a stretching cylinder. Ellahi *et al.* [26] illustrated the entropy of HNF MHD flow through porous media. Dalir *et al.* [27] evaluated the entropy of Jeffrey fluid. Shah *et al.* [28] analysed the mathematical modelling of entropy based on several NPs. Raja *et al.* [29] explored the concept of computational modelling of neural networks for entropy. Qasim and Afridi [30], Mahdavi *et al.* [31], and Khan *et al.* [32,33] investigated several factors affecting the entropy conversion.

The interfacial nanolayer of the NPs is a thin structure layer at the interface of the NP surface. Interfacial nanolayer thickness of NPs is a valuable feature to control the

thermal conductivity of the NPs and embedded base fluid [34,35]. An improvement in the thermal conductivity of the NFs was observed in the presence of a larger nanolayer thickness of the NPs [36,37]. Zeroual *et al.* [38] showed that the viscosity of NFs improved with enhancement in the ordered liquid layer. Yu and Choi [39] used a renovated Maxwell model to show the impact of the interfacial nanolayer. The analysis was based on two different nanolayer thicknesses and shows that the thermal conductivity of the NF considerably improved even with a very thin nanolayer, exclusively when the diameter of the particle was less than 10 nm. A solid–liquid interface with molecular-level layering shows a significant impact on the interaction of dynamic NPs [40]. Khodayari *et al.* [41] discussed different models for the outcome of the interfacial nanolayers and their impact on the thermal conductivity of the NFs. Enhancing viscosity and thermal conductivity with the interfacial nanolayer structure of the NPs has been observed by Li *et al.* [42]. Recently, many researchers succeeded in determining the significance of the nanolayer thickness on the thermal properties by optical experimental measurements [43] or by molecular dynamics replications [44–46]. Fan and Zhong [47] have discussed the impact of microparameters on the thickness of the interfacial nanolayer and its significance for the thermal properties of the NPs and NFs. Gkountas *et al.* [48] have discussed the consequence of the NP interface layer on heat transfer by considering $Al_2O_3$. Tillman and Hill [49] have discussed how the thermal conductivity of the NP influences the change in nanolayer thickness. Kumar *et al.* [50] examined the consequences of interfacial nanolayers by using hybrid NPs within a squeezing channel. Jiang *et al.* [51–53] exploited the convective heat extensions to investigate single- and MWCNTs submerging a non-Darcy porous medium with water-based NF flow on discs. Gowda *et al.* [54–56] assessed the impact of an interfacial nanolayer on a curved stretched sheet with convective boundary conditions.

The above literature inspired the researchers to analyse the importance of the thickness of the interfacial nanolayer and Marangoni convection on heat transfer. The present study analyzes the importance of the steady Darcy-Forchheimer MWCNT-$MoS_2$/blood HNF flow under a permeable disk. The foremost objectives are to (a) analyse the perception of an interfacial nanolayer thickness, which illustrates an inclusive importance on the thermos-physical properties of NFs; (b) evaluate the presentation of exponential heat generation, non-linear thermal radiation, and Joule heating on the thermal control of the system; (c) analyse the thermo-solutal Marangoni convection with activation energy; and (d) examine the entropy and thermal effectiveness on the typical system.

The novelties of the present study include the following:

- Analyse the thermo-solutal Marangoni convective Darcy-Forchheimer MWCNT-$MoS_2$/blood hybrid bio-fluid flow over a stretching rotating disk.
- Analyse the interfacial mechanism of the NPs and its impact on the flow and thermal feature.
- A potential numerical technique G-FEM method was applied to solve the governing equations.
- Analyse the entropy optimisation of HNFs subject to radially revolved flow.

The motive of the research is to interpret the HNF flow over base fluid blood on the spinning disk based on interfacial nanolayer NPs, as it has enormous utility in different industries and medical sciences mainly bio-reactor.

## 2 Mathematical formulation

Assume that the thermos-solutal Marangoni convective Darcy-Forchheimer bio-HNF (accumulation of MWCNT and $MoS_2$ into the base fluid blood) flows over a permeable disk with spin angular velocity nanomaterials $\Omega$ (Figure 1). The Darcy-Forchheimer model is expressed as a viscous 2D stable, incompressible fluid in a porous surface area. A constant magnetic field acts in the direction of motion. The energy equation takes into account thermal radiation, exponential heat generation, and viscous dissipation. The concentration equation includes activation energy from a binary chemical process [57–59].

Using the above assumptions, the mathematical model can be characterised as follows [60–62]:

$$\frac{\partial u}{\partial r} + \frac{u}{r} + \frac{\partial w}{\partial z} = 0, \tag{1}$$

$$\left(u\frac{\partial u}{\partial r} + w\frac{\partial u}{\partial z}\right) = \frac{\mu_{\mathrm{hnf}}}{\rho_{\mathrm{hnf}}}\frac{\partial^2 u}{\partial z^2} - \frac{\mu_{\mathrm{hnf}}}{\rho_{\mathrm{hnf}}K_{\mathrm{p}}}u - \frac{C_{\mathrm{b}}}{\sqrt{K_{\mathrm{p}}}}u^2 - \frac{\sigma_{\mathrm{hnf}}}{\rho_{\mathrm{hnf}}}B_0^2 u, \tag{2}$$

$$\left(u\frac{\partial T}{\partial r} + w\frac{\partial T}{\partial z}\right) = \left(\frac{k_{\mathrm{hnf}}}{(\rho C_{\mathrm{p}})_{\mathrm{hnf}}} + \frac{16\sigma^* T_\infty{}^3}{3k^*(\rho c_{\mathrm{p}})_{\mathrm{hnf}}}\right)\frac{\partial^2 T}{\partial z^2} + \frac{1}{(\rho C_{\mathrm{p}})_{\mathrm{hnf}}}Q_0(T - T_\infty)\exp\left(-n\sqrt{\frac{\Omega}{\nu_{\mathrm{f}}}}z\right) + \frac{\mu_{\mathrm{hnf}}}{(\rho C_{\mathrm{p}})_{\mathrm{hnf}}}\left(\frac{\partial u}{\partial z}\right)^2, \tag{3}$$

$$u\frac{\partial C}{\partial r} + w\frac{\partial C}{\partial z} = D_{\mathrm{B}}\frac{\partial^2 C}{\partial z^2} - K_0{}^2(C - C_\infty)\left(\frac{T}{T_\infty}\right)^n \exp\left(\frac{-E_{\mathrm{a}}}{kT}\right). \tag{4}$$

Eq. (1) represents the continuity equation (conservation of mass). Momentum equation is represented by Eq. (2) with the second term on the right-hand side representing the

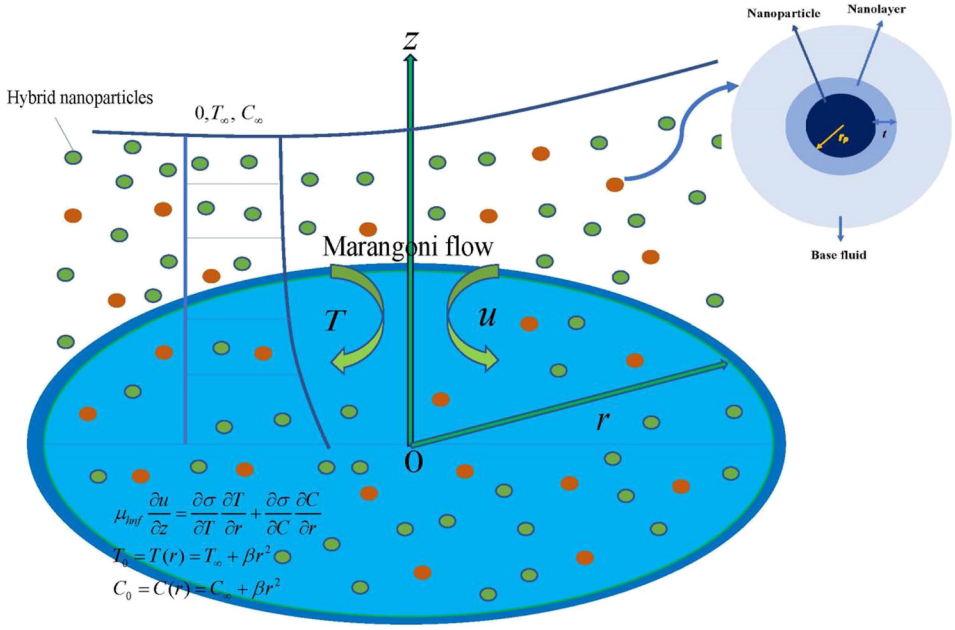


**Figure 1:** Geometry of the problem.

porous medium, third term representing Darcy-Forchheimer flow phenomena, and the last term is due to the magnetic force. Eq. (3) is the energy equation with the first term on the right-hand side representing thermal radiation, second term representing the exponential heat generation, and the last term relates with the viscous dissipation. Eq. (4) represents the concentration equation with the last term on the right-hand side being binary chemical reaction with the activation energy.

The boundary conditions of the article are represented as follows [1,4]:

$$\left.\begin{aligned} &\mu_{\text{hnf}}\frac{\partial u}{\partial z}\bigg|_{Z=0} = \frac{\partial \sigma}{\partial z}\bigg|_{Z=0} = \frac{\partial \sigma}{\partial T}\frac{\partial T}{\partial r}\bigg|_{Z=0} + \frac{\partial \sigma}{\partial C}\frac{\partial C}{\partial r}\bigg|_{Z=0},\\ &T|_{Z=0} = T_0 = T_\infty + \beta r^2, C|_{Z=0} = C_0 = C_\infty + \beta r^2,\\ &u|_{z\to\infty} = 0, T|_{Z\to\infty} = T_\infty, C|_{Z\to\infty} = C_\infty. \end{aligned}\right\} \tag{5}$$

with $\sigma = \sigma_0[(1 - \gamma_T(T - T_\infty) - \gamma_C(C - C_\infty)]$, where $\gamma_T = \frac{-1}{\sigma_0}\frac{\partial \sigma}{\partial T}\Big|_{T=T_\infty}$ and $\gamma_C = \frac{-1}{\sigma_0}\frac{\partial \sigma}{\partial C}\Big|_{C=C_\infty}$.

The boundary conditions at the surface defined the Marangoni convection condition subject to thermal and solutal impact of the surface tensions with a temperature and concentration slip at the surface. Zero velocity with the ambient temperature and concentration are defined at the boundary layer. Here $T$ is the temperature of the fluid within the boundary layer, $\sigma^*$ is the Stefan Boltzmann constant, $k^*$ is the mean absorption coefficient, $\gamma_T$ represents the coefficient of temperature surface tension, $\gamma_C$ represents the coefficient of concentration surface tension, and $\sigma_0$ is a positive constant.

The transformations executed for the existing problem include [1]

$$\left.\begin{aligned} &\eta = \sqrt{\frac{\Omega}{\upsilon_f}}\, z,\ (u, w) = (r\Omega F(\eta), -\sqrt{\Omega \upsilon_f}\, H(\eta)),\\ &(T, C) = (T_\infty + \beta r^2\theta(\eta), C_\infty + \beta r^2\phi(\eta)), \end{aligned}\right\} \tag{6}$$

where $\eta$ is considered as the rotation of the axis. Additionally, $F$, $H$, $\theta$, and $\phi$ are functions of $\eta$.

Taking the help of Eq. (6), Eqs. (1)–(5) take the form

$$2F + H' = 0, \tag{7}$$

$$\frac{1}{\varepsilon_1\varepsilon_2}(2F'' - \lambda F) - F^2 + HF' + (1 + \text{Fr})F'^2 + \varepsilon_4 MF = 0, \tag{8}$$

$$\begin{aligned} &\frac{1}{\text{Pr}}\left(\frac{k_{\text{hnf}}}{k_f} + \frac{4}{3}\text{Rd}\right)\theta'' + \frac{\text{Rd}}{\text{Pr}}\{3(\theta_w - 1)((\theta_w - 1)\theta + 1)^2\theta'\\ &\quad + \theta''(1 + (\theta_w - 1))^3\}^2 - 2\varepsilon_3(F\theta + \theta' H)\\ &\quad + Q_T\theta\exp(-n\eta) + \frac{1}{\varepsilon_1}E_c F'^2 = 0, \end{aligned} \tag{9}$$

$$\frac{1}{S_c}\phi'' + 2F\phi' + H\phi - K_1(1 + \theta_w\theta)^n \exp\left(\frac{-E_1}{1 + \theta_w\theta}\right) = 0, \tag{10}$$

$$\left.\begin{aligned} &F'(\eta)|_{\eta=0} = -2(1 + r^*)\varepsilon_1,\ H(\eta)|_{\eta=0} = 0,\\ &\theta(\eta)|_{\eta=0} = 1, \phi(\eta)|_{\eta=0} = 1,\\ &F'(\eta)|_{\eta=\infty} = 0, \theta(\eta)|_{\eta=\infty} = 0, \phi(\eta)|_{\eta=\infty} = 0. \end{aligned}\right\} \tag{11}$$

With the parameters

$$\left.\begin{aligned} r^* &= \frac{C_0\gamma_C}{T_0\gamma_T},\ \mathrm{Re}_r=\left(\frac{r^2\Omega}{\upsilon_f}\right),\ F_r = \frac{rC_b}{\sqrt{K_p}}, M = \frac{\sigma_f B_0^2}{\rho_f\Omega},\\ \mathrm{Ec} &= \frac{r^2\Omega}{\beta(C_p)_f},\\ Q_T &= \frac{Q_0}{\Omega(\rho c_p)_f},\ \theta_w = \frac{T_0 - T_\infty}{T_\infty}, \lambda = \frac{\upsilon_f}{\Omega K_p},\\ \mathrm{Pr} &= \frac{(\mu C_P)_f}{K_f}, \mathrm{Br} = \mathrm{Pr}\,\mathrm{Ec},\\ \mathrm{Rd} &= \frac{4\sigma^* T_\infty^3}{k^* k_f},\ K_1 = \frac{\Omega {K_0}^2}{\upsilon_f},\ S_c = \frac{\upsilon_f}{D_B}, E_1 = \frac{E_a}{KT}. \end{aligned}\right\} \quad (12)$$

and

$$\varepsilon_1 = \frac{\mu_f}{\mu_{hnf}},\ \varepsilon_2 = \frac{\rho_{hnf}}{\rho_f},\ \varepsilon_3 = \frac{(\rho c_p)_{hnf}}{(\rho c_p)_f},\ \varepsilon_4 = \frac{\sigma_{hnf}}{\sigma_f}, \quad (13)$$

The skin friction can be formed as follows:

$$(\mathrm{Re}_r)^{1/2} C_{fr} = \frac{1}{\varepsilon_1}\{\sqrt{[F'(0)]^2 + [H'(0)]^2}\}. \quad (14)$$

The Nusselt number can be formed as follows:

$$(\mathrm{Re}_r)^{-1/2}\mathrm{Nu}_r = -\left(\frac{k_{hnf}}{k_f} + \frac{4}{3}\mathrm{Rd}\{1 + (\theta_w - 1)\theta(0)\}^3\right)\theta'(0). \quad (15)$$

The Sherwood number can be formed as follows:

$$(\mathrm{Re}_r)^{-1/2}\mathrm{Sh}_r = -\phi'(0). \quad (16)$$

## 2.1 Entropy model

The entropy based on NF is specified by

$$\begin{aligned} \dot{S}_G = {} & \frac{k_{nf}}{T_\infty^2}\left[\frac{k_{hnf}}{k_f} + \frac{4}{3}\mathrm{Rd}\right]\left\{\left(\frac{\partial T}{\partial z}\right)^2 + \frac{\mu_{nf}}{T_\infty}\left\{\left(\frac{\partial u}{\partial z}\right)^2\right\}\right.\\ & + \frac{\mu_{hnf}}{T_\infty K^*}(u^2 + w^2)\\ & \left. + \frac{R^* D_B}{T_\infty}\left(\frac{\partial T}{\partial z}\right)\left(\frac{\partial C}{\partial z}\right) + \frac{R^* D_B}{C_\infty}\left(\frac{\partial C}{\partial z}\right)^2\right\}. \end{aligned} \quad (17)$$

The non-dimensional entropy rate $N_G$ becomes

$$\begin{aligned} N_G = {} & \left(\frac{k_{hnf}}{k_f} + \frac{4}{3}\mathrm{Rd}\right)\theta'^2 + \mathrm{Br}\,\mathrm{Re}_r F'^2 + \mathrm{Br}\,K(F^2 + H^2)\\ & + L^*\theta'\phi' + L^*\frac{\theta_w}{\theta}\phi'^2, \end{aligned} \quad (18)$$

with $\mathrm{Br} = \frac{\mu_{nf}\Omega\upsilon_f}{k_{nf}\beta^2 r^4}$, $\mathrm{Re}_r = \frac{\Omega r^2}{\upsilon_f}$, $N_G = \frac{\dot{S}_G}{\left(\frac{k_{nf}}{T_\infty^2}\frac{\Omega}{\upsilon_f}\beta^2 r^4\right)}$, and $L^* = \frac{R^* D_B}{k_{nf}}$.

The Bejan number is demonstrated as

$$\mathrm{Be} = \frac{\left(\frac{k_{hnf}}{k_f} + \frac{4}{3}\mathrm{Rd}\right)\theta'^2}{\left(\frac{k_{hnf}}{k_f} + \frac{4}{3}\mathrm{Rd}\right)\theta'^2 + \mathrm{Br}\,\mathrm{Re}_r F'^2 + \mathrm{Br}\,K(F^2 + H^2) + L^*\theta'\phi' + L^*\frac{\theta_w}{\theta}\phi'^2}. \quad (19)$$

## 2.2 Improved thermophysical properties due to interfacial nanolayer

Schwartz *et al.* [63–65] have shown the thermal conductivity by using Maxwell model

$$k_{improve} = \frac{[2(1-\gamma) + (1-\beta)^3(1+2\gamma)]\gamma}{(1-\beta)^3(1+2\gamma) - (1-\gamma)}k_p, \quad (20)$$

where $\gamma = k_{layer}/k_p$ is the ratio between the nanolayer thermal conductivity ($k_{layer}$) and NP thermal conductivity ($k_p$). Yu and Choi [39,66] have used a renovated Maxwell model and showed that the improved volume fraction of the NPs $\phi_{improve}$ can be written as $\phi_{improve} = \phi(1+\beta)^3$ for the radius of the NP $r_p$ and ratio $\beta = t/r_p$ with encompassing nanolayer thickness $t$ and improved the Maxwell model as follows:

$$k_{improve} = \frac{k_p + 2k_f + 2(k_p - k_f)(1+\beta)^3\phi}{k_p + 2k_f - (k_p - k_f)(1+\beta)^3\phi}k_f. \quad (21)$$

Later, Leong *et al.* [66] and Xie *et al.* [67] modified the thermal conductivity of the NF with the engagement of the interfacial nanolayer thickness of the NPs. All the above works are based on the concept of the NF. Jiang *et al.* [34] showed the role of the interfacial nanolayer and its influence on upgrading the thermal conductivity of the CNT-based NF. This concept was further extended for the HNF, and the thermophysical features of the NPs improved with the influence of the interfacial nanolayer. Because of the appearance of the interfacial nanolayers, an upgrade in NP and volume fraction is observed [50,68].

$$\phi_1 = (1 + I_{MWCNT})^2\phi_{MWCNT},\ \phi_2 = (1 + I_{MoS_2})^2\phi_{MoS_2}, \quad (22)$$

where $\phi_1$, $\phi_2$ are the updated volume fractions, and $\phi_{MWCNT}$, $\phi_{MoS_2}$ are the initial volume fractions with the interfacial ratio parameter $I_{MWCNT}$, $\phi_{MoS_2}$ described by the proportion of the width of the nanolayer to the radius of the NPs for MWCNT and $MoS_2$.

Physical parameters are upgraded for the HNF as follows:

$$
\begin{aligned}
\mu_{\mathrm{hnf}} &= \mu_f(1-\phi_{\mathrm{MWCNT}})^{-2.5}(1-\phi_{\mathrm{MoS_2}})^{-2.5},\\
\rho_{\mathrm{hnf}} &= (1-\phi_{\mathrm{MoS_2}})[(1-\phi_{\mathrm{MWCNT}})\rho_{\mathrm{f}}+\phi_{\mathrm{MWCNT}}\rho_{\mathrm{MWCNT}}]\\
&\quad+\phi_{\mathrm{MoS_2}}\rho_{\mathrm{MoS_2}},\\
(\rho c_{\mathrm{p}})_{\mathrm{hnf}} &= (1-\phi_{\mathrm{MoS_2}})[(1-\phi_{\mathrm{MWCNT}})(\rho c_{\mathrm{p}})_{\mathrm{f}}\\
&\quad+\phi_{\mathrm{MWCNT}}(\rho c_{\mathrm{p}})_{\mathrm{MWCNT}}]+\phi_{\mathrm{MoS_2}}(\rho c_{\mathrm{p}})_{\mathrm{MoS_2}},\\
\sigma_{\mathrm{hnf}} &= (1-\phi_{\mathrm{MoS_2}})[(1-\phi_{\mathrm{MWCNT}})\sigma_{\mathrm{f}}+\phi_{\mathrm{MWCNT}}\sigma_{\mathrm{MWCNT}}]\\
&\quad+\phi_{\mathrm{MoS_2}}\sigma_{\mathrm{MoS_2}},\\
(\rho\beta)_{\mathrm{hnf}} &= (1-\phi_{\mathrm{MoS_2}})[(1-\phi_{\mathrm{MWCNT}})(\rho\beta)_{\mathrm{f}}\\
&\quad+\phi_{\mathrm{MWCNT}}(\rho\beta)_{\mathrm{MWCNT}}]+\phi_{\mathrm{MoS_2}}(\rho\beta)_{\mathrm{MoS_2}}.
\end{aligned}
\tag{23}
$$

Thermal conductivity of MWCNT ($\zeta_1$) and $MoS_2$ ($\zeta_2$) improved as follows:

$$
\begin{aligned}
\zeta_{\mathrm{MWCNT}} &= \frac{(1+I_{\mathrm{MWCNT}})k_{\mathrm{MWCNT}}-k_{\mathrm{f}}}{I_{MWCNT}k_{\mathrm{f}}}\\
&\quad\times\frac{\ln(1+I_{\mathrm{MWCNT}})}{\ln[(1+I_{\mathrm{MWCNT}})k_{\mathrm{MWCNT}}/k_{\mathrm{f}}]},\\
\zeta_{\mathrm{MoS_2}} &= \frac{(1+I_{\mathrm{MoS_2}})k_{\mathrm{MoS_2}}-k_{\mathrm{f}}}{I_{\mathrm{MoS_2}}k_{\mathrm{f}}}\frac{\ln(1+I_{\mathrm{MoS_2}})}{\ln[(1+I_{\mathrm{MoS_2}})k_{\mathrm{MoS_2}}/k_{\mathrm{f}}]},
\end{aligned}
\tag{24}
$$

which further improved the composite thermal conductivity of MWCNT ($\tau_{\mathrm{MWCNT}}$) and $MoS_2$ ($\tau_{\mathrm{MoS_2}}$) as follows:

$$
\begin{aligned}
&\tau_{\mathrm{MWCNT}}\\
&=\frac{2k_{\mathrm{MWCNT}}+[(1+I_{\mathrm{MWCNT}})^2-1](k_{\mathrm{MWCNT}}+\zeta_{\mathrm{MWCNT}})}{2\zeta_{\mathrm{MWCNT}}+[(1+I_{\mathrm{MWCNT}})^2-1](k_{\mathrm{MWCNT}}+\zeta_{\mathrm{MWCNT}})}\\
&\quad\times\zeta_{\mathrm{MWCNT}},\\
&\tau_{\mathrm{MoS_2}}=\frac{2k_{\mathrm{MoS_2}}+[(1+I_{\mathrm{MoS_2}})^2-1](k_{\mathrm{MoS_2}}+\zeta_{\mathrm{MoS_2}})}{2\zeta_{\mathrm{MoS_2}}+[(1+I_{\mathrm{MoS_2}})^2-1](k_{\mathrm{MoS_2}}+\zeta_{\mathrm{MoS_2}})}\zeta_{\mathrm{MoS_2}},
\end{aligned}
\tag{25}
$$

where $k_{\mathrm{MWCNT}}$, $k_{\mathrm{MoS_2}}$ and $k_{\mathrm{f}}$ are the original thermal conductivities of MWCNT, $MoS_2$, and base fluid blood.

By employing the properties of revised composite NPs, the effective thermal conductivity of HNF is as follows [57]:

$$
k_{\mathrm{hnf}}=\frac{\tau_{\mathrm{MoS_2}}+(n-1)k_{\mathrm{nf}}+(n-1)(\tau_{\mathrm{MoS_2}}-k_{\mathrm{nf}})\varphi_{\mathrm{MoS_2}}}{\tau_{\mathrm{MoS_2}}+(n-1)k_{\mathrm{nf}}-(\tau_{\mathrm{MoS_2}}-k_{\mathrm{nf}})\varphi_{\mathrm{MoS_2}}}k_{\mathrm{nf}},
\tag{26}
$$

with

$$
k_{\mathrm{nf}}=\frac{\tau_{\mathrm{MWCNT}}+(n-1)k_{\mathrm{f}}+(n-1)(\tau_{\mathrm{MWCNT}}-k_{\mathrm{f}})\varphi_{\mathrm{MWCNT}}}{\tau_{\mathrm{MWCNT}}+(n-1)k_{\mathrm{f}}-(\tau_{\mathrm{MWCNT}}-k_{\mathrm{f}})\varphi_{\mathrm{MWCNT}}}k_{\mathrm{f}}.
$$

# 3 Methodology

The mathematical approach of the Galerkin finite element scheme is concerned with resolving the reduced leading Eqs. (7)–(10) with the help of Eq. (11). Some major steps for G-FEM solutions include the conversion of partial differential equations into sets of ordinary differential equations and the formation of residuals.

Step 1:

By breaking the problem domain down into its component parts, the subdomains are acquired. Instead of providing an approximate solution across the entire domain, the discretisation of the elements provides an approximation solution over each element, and the approximation solution is seen as a linear polynomial. Weighted residuals are derived as follows:

$$
\int_{\eta_{\mathrm{e}}}^{\eta_{\mathrm{e}+1}} w_1[F'-H]\,\mathrm{d}\eta=0,
\tag{27}
$$

$$
\int_{\eta_{\mathrm{e}}}^{\eta_{\mathrm{e}+1}} w_2\left[\frac{1}{\varepsilon_1\varepsilon_2}(2H'-\lambda F)-F^2+H^2+(1+\mathrm{Fr})H^2+\varepsilon_4\mathrm{MF}\right]\mathrm{d}\eta=0,
\tag{28}
$$

$$
\int_{\eta_{\mathrm{e}}}^{\eta_{\mathrm{e}+1}} w_3\left[\begin{array}{l}\frac{1}{\mathrm{Pr}}\left(\frac{k_{\mathrm{hnf}}}{k_{\mathrm{f}}}+\frac{4}{3}\mathrm{Rd}\right)\theta''\\ +\frac{\mathrm{Rd}}{\mathrm{Pr}}\{3(\theta_{\mathrm{w}}-1)((\theta_{\mathrm{w}}-1)\theta+1)^2\theta'+\theta''(1+(\theta_{\mathrm{w}}-1))^3\}^2\\ -2\varepsilon_3(F\theta+\theta' H)+Q_1\theta\exp(-n\eta)+\frac{1}{\varepsilon_1}\mathrm{Ec}\,H^2\end{array}\right]\mathrm{d}\eta=0,
\tag{29}
$$

$$
\int_{\eta_{\mathrm{e}}}^{\eta_{\mathrm{e}+1}} w_4\left[\frac{1}{\mathrm{Sc}}\phi''+2F\phi'+H\phi-K_1\left(1+\frac{1}{\theta_{\mathrm{w}}}\right)^n\exp\left(\frac{-E_1}{1+\theta_{\mathrm{w}}}\right)\right]\mathrm{d}\eta=0.
\tag{30}
$$

Step 2:

The orthogonal nodal basis with the Kronecker delta property serves as the foundation for the shape functions. The product of shape functions yields the approximate solution. Here we employ the linear shape functions.

Step 3:

In order to establish stiffness elements and a global stiffness matrix, this numerical scheme is calculated. Stiffness elements are given by

$$
K_{ij}^{11}=\left(\frac{\mathrm{d}\psi_j}{\mathrm{d}\eta}\psi_i\right),\ b_i^1=0,\ K_{ij}^{12}=-(\psi_i\psi_j)\mathrm{d}\eta,\ K_{ij}^{13}=0,\ K_{ij}^{14}=0,
\tag{31}
$$

$$
K_{ij}^{22}=\left[\frac{1}{\varepsilon_1\varepsilon_2}\left(2\psi_i\frac{\mathrm{d}\psi_i}{\mathrm{d}\eta}-\lambda F\right)-F^2+H\psi_i\psi_j+(1+\mathrm{Fr})(\psi_i\psi_j)^2+\varepsilon_4\mathrm{MF}\right]\mathrm{d}\eta,
\tag{32}
$$

$$
b_i^2=0,\ K_{ij}^{23}=[\lambda_N\psi_i\psi_j]\mathrm{d}\eta,\ K_{ij}^{24}=[\lambda_M\psi_i\psi_j]\mathrm{d}\eta,
\tag{33}
$$

$$b_i^3 = 0, K_{ij}^{31} = 0, K_{ij}^{32} = 0,$$

$$K_{ij}^{33} = \begin{bmatrix} -\frac{1}{\mathrm{Pr}}\left(\frac{k_{\mathrm{hnf}}}{k_{\mathrm{f}}} + \frac{4}{3}\mathrm{Rd}\right)\frac{\mathrm{d}\psi_i}{\mathrm{d}\eta}\frac{\mathrm{d}\psi_j}{\mathrm{d}\eta} \\ + \frac{\mathrm{Rd}}{\mathrm{Pr}} \\ \left\{3(\theta_{\mathrm{w}}-1)((\theta_{\mathrm{w}}-1)\psi_i\psi_j+1)^2\frac{\mathrm{d}\psi_j}{\mathrm{d}\eta}\psi_i\right\}^2 \\ +\frac{\mathrm{d}\psi_i}{\mathrm{d}\eta}\frac{\mathrm{d}\psi_j}{\mathrm{d}\eta}(1+(\theta_{\mathrm{w}}-1))^3 \\ -2\varepsilon_3\left(F\psi_i\psi_j + \frac{\mathrm{d}\psi_j}{\mathrm{d}\eta}\psi_i H\right) + Q_{\mathrm{T}}\psi_i\psi_j\exp(-n\eta) \\ + \frac{1}{\varepsilon_1}\mathrm{Ec}\,H^2 \end{bmatrix}\mathrm{d}\eta, \quad (34)$$

$$K_{ij}^{34} = \frac{1}{\varepsilon_1}\mathrm{Ec}\,H^2, b_i^4 = 0, K_{ij}^{41} = 0, K_{ij}^{42} = 0,$$

$$K_{ij}^{43} = \left[-K_1\left(1+\frac{1}{\theta_w}\right)^n \exp\left(\frac{-E_1}{1+\theta_{\mathrm{w}}}\right)\right]\mathrm{d}\eta,$$

$$K_{ij}^{44} = \left[-\frac{1}{\mathrm{Sc}}\frac{\mathrm{d}\psi_i}{\mathrm{d}\eta}\frac{\mathrm{d}\psi_j}{\mathrm{d}\eta} + 2F\frac{\mathrm{d}\psi_j}{\mathrm{d}\eta}\psi_i + H\psi_i\psi_j - K_1\left(1+\frac{1}{\theta_{\mathrm{w}}}\right)^n \exp\left(\frac{-E_1}{1+\theta_{\mathrm{w}}}\right)\right]\mathrm{d}\eta. \quad (35)$$

Step 4:

Global stiffness matrix is obtained with the help of the assembly process. With the help of Picard's linearisation approach, the nonlinear equations are formed. The convergence analysis is done. Nonlinear equations are simulated through the computational tolerance ($10^{-5}$) with the criteria $\left|\frac{x_{i+1}-x_i}{x^i}\right| \langle 10^{-5}$.

# 4 Results and discussion

The thermophysical properties of the nanoparticles and base fluid are given in Table 1. A flow map of the solution process has been explained in Figure 2. The induction of the different significant features on velocity, temperature, and concentration along with such physical quantities as skin friction, Nusselt number, and Sherwood number has been exhibited through graphs. Further, the consequences of different factors on the entropy with Bejan number are revealed *via* graphs. The overall results of the parameter are taken as $M = 2$, $K = 0.5$, Rd = 1.0, Ma = 0.3, Ec = 0.5, Fr = 0.5, $Q_{\mathrm{T}} = 0.2$, Pr = 7, $\theta_{\mathrm{w}} = 0.9$, Sc = 10, $K_1 = 1.2$, $E_1 = 1.5$, and Br = 0.3.

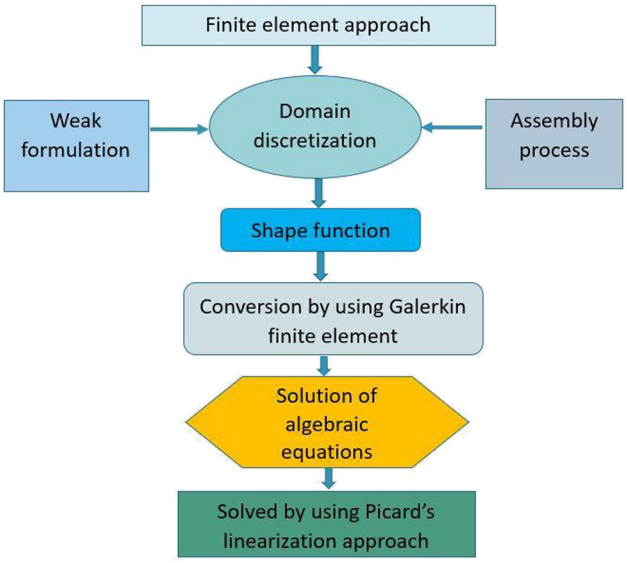


**Figure 2:** The flow chart of the solution procedure.

## 4.1 Velocity distribution

Figure 3 illustrates that the velocity of the HNF diminished with an enhancement in the magnetic parameters. Physically, a Lorentz force is created in the presence of the magnetic field, which opposes the fluid motion. In each case, we made a comparison between the mono NF (NF with a single NP) and the HNF (NF with dual NPs). Also, we have discussed the importance of the interfacial nanolayer thickness of the NPs. In the present problem, we have considered two sets of nanolayer thicknesses, namely, $I_1 = I_2 = 0.01$ and $I_1 = I_2 = 0.03$. The velocity profile observed declined more in the presence of dual NPs in the base fluid than in the presence of a single

**Table 1:** Thermophysical properties of the nanoparticles and base fluid

| | $\rho$(kg/m$^3$) | $c_{\mathrm{p}}$(J/kg K) | $k$(W/mK) | $\beta$(K$^{-1}$) | $\sigma(\Omega^{-1}$ m$^{-1})$ |
|---|---|---|---|---|---|
| Blood | 1,050 | 3617 | 0.52 | $0.18 \times 10^{-5}$ | 0.8 |
| MWCNT | 1,600 | 796 | 3,000 | $2 \times 10^{-5}$ | $1 \times 10^{7}$ |
| $MoS_2$ | 5,060 | 397.21 | 904.4 | $2.8424 \times 10^{-5}$ | $2.09 \times 10^{4}$ |

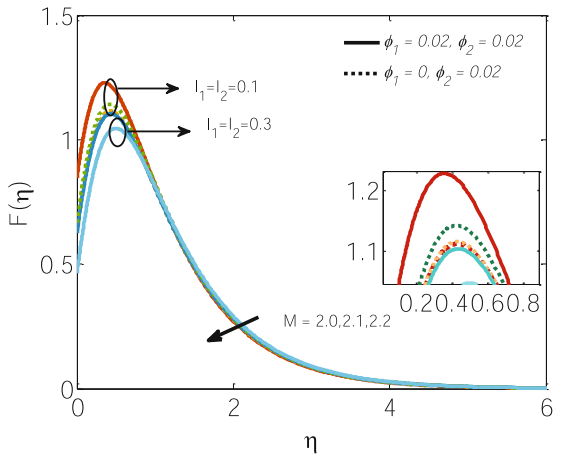


**Figure 3:** Velocity profile for different $M$ with a comparison of NF and HNF with the impact of interfacial nanolayer thickness.

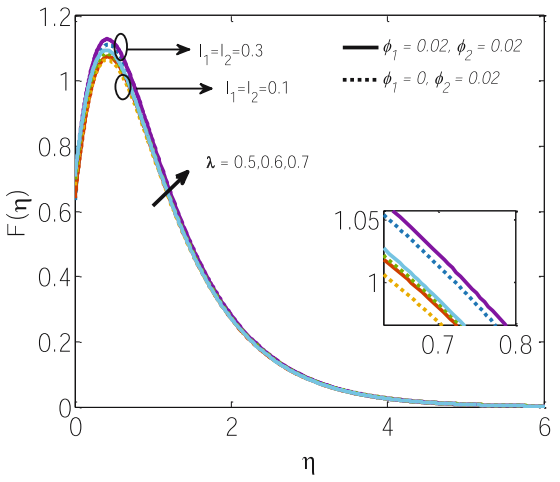


**Figure 5:** Velocity profile for different $\lambda$ with a comparison of NF and HNF with the impact of interfacial nanolayer thickness.

NP. It may be due to the advanced value in viscosity, which is larger in the presence of dual NPs. Moreover, the velocity slows down with an increase in the width of the interfacial nanolayers of the NPs, which are mainly used during the preparation of NPs. The consequence of the Marangoni parameter on the velocity profiles of both fluids is shown in Figure 4. The Marangoni effect appears due to gradients in surface tension, which add a resistive force to the system, resulting in a reduced velocity as well as a reduced momentum boundary layer thickness. Figure 5 indicates that the velocity profile declined with an improved value of the porosity variable $\lambda$. This is due to the fact that the fluid has more room to flow with better performance of the porosity variable, which slows down the velocity at the surface. The outcomes of non-uniform inertia coefficients on the velocity distribution are observed in Figure 6. A decline in velocity distribution is observed with larger values of Fr, when the nonlinear inertia Fr is 1, as opposed to 1.5, which has less impact and reduces the momentum boundary layer thickness for both the nanofluid and HNF. When the velocity decreases, the molecules of the liquid become less active and less rapid due to the presence of $\sqrt{K_p}$. A similar observation was found by Ullah [1].

## 4.2 Temperature distribution

Figure 7 represents the temperature distribution for different values of Rd, radiation parameter. This indicates that the thermal boundary layer thickness improves with larger values of Rd. Radiation acts as an external source

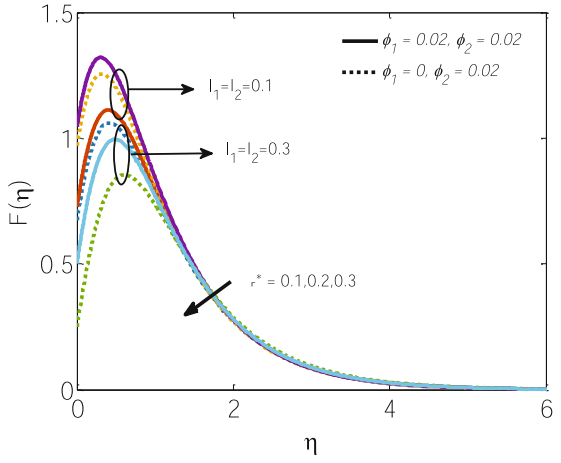


**Figure 4:** Velocity profile for different $r^*$ with a comparison of NF and HNF with the impact of interfacial nanolayer thickness.

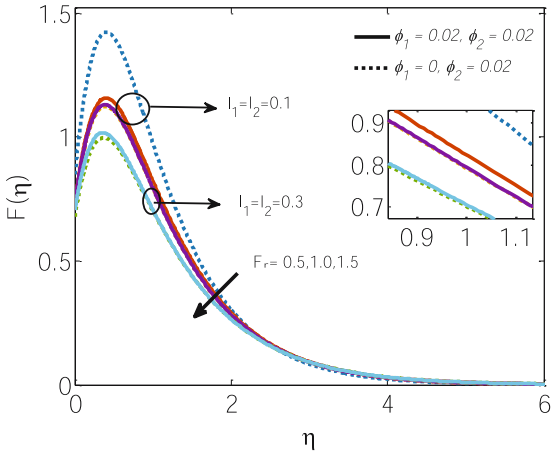


**Figure 6:** Velocity profile for different Fr with a comparison of NF and HNF with the impact of interfacial nanolayer thickness.

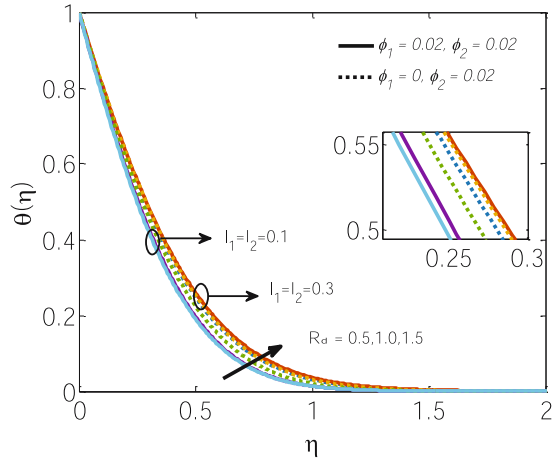


**Figure 7:** Temperature profile for different Rd with a comparison of NF and HNF with the impact of interfacial nanolayer thickness.

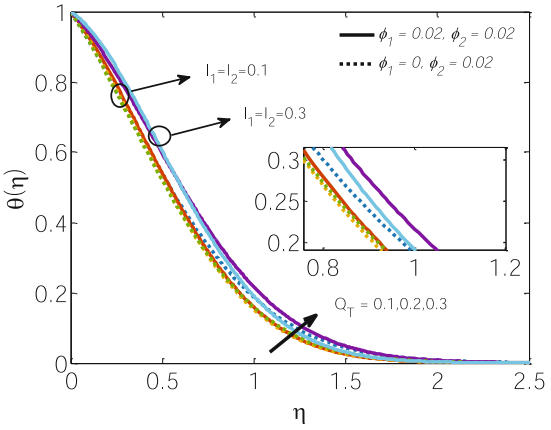


**Figure 9:** Temperature profile for different $Q_T$ with a comparison of NF and HNF with the impact of interfacial nanolayer thickness.

which supplies additional external heat to the system. Physically heat is created within the liquid MWCNT and $MoS_2$due to the presence of $\sigma^* T_\infty^3$. As Rd increases within the range of $0 \le Rd \le 1$, the temperature distribution increases significantly along $0 \le \eta \le 2$, afterward the temperature of both NF and HNF saturate at zero to follow the boundary condition. A similar phenomenon was observed by Madhukesh *et al.* [24]. In the temperature profiles, a comparison of the HNF and general NF has been observed. In all figures, it is observed that the presence of the dual NPs in the system generates more heat than the appearance of a single NP, and this is due to the dominant thermal properties of NPs. Hence, a higher temperature is observed in the presence of dual NPs (HNF) than mono NPs (NF). As a result, the thermal boundary layer thickness is larger in the presence of dual NPs than mono NPs in the base fluid blood. Also, a comparison was made with the thickness of the interfacial nanolayers for each graph. It was observed that an expansion in the interfacial nanolayer thickness of the NPs restricted the temperature at the surface and simultaneously in the system. Figure 8 illustrates how the magnetic field coefficient $M$ affects the temperature distribution. From the figure, it is noticeable that with enhanced values of $M$, the temperature rises substantially in the wall and surrounding area. It is observed from Figure 9 that an improvement in the heat generation parameter enhances the thermal boundary layer thickness of the system. It is because, with a rise in heat generation, the consistent forces diminish with improved molecular thermal activity. Figure 10 shows that the temperature increased with an increase in the value of Ec. A comparable feature was supported by the work of Mahanthesh *et al.* [4] for the temperature profile as a function of Ec. An impact of the

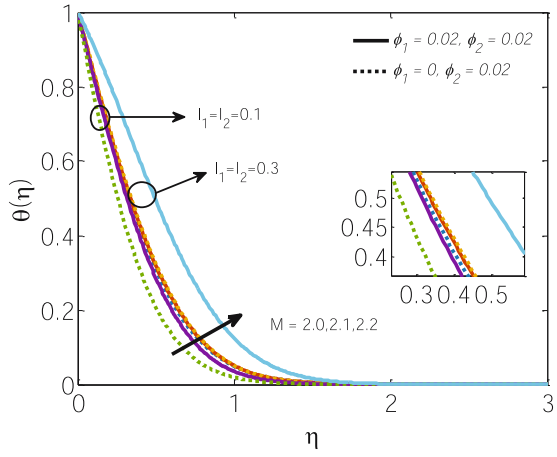


**Figure 8:** Temperature profile for different $M$ with a comparison of NF and HNF with the impact of interfacial nanolayer thickness.

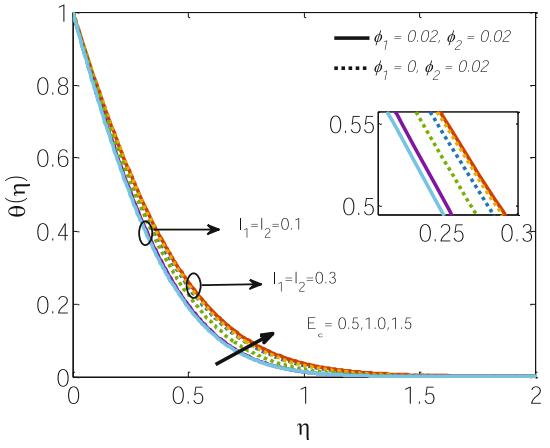


**Figure 10:** Temperature profile for different Ec with a comparison of NF and HNF with the impact of interfacial nanolayer thickness.

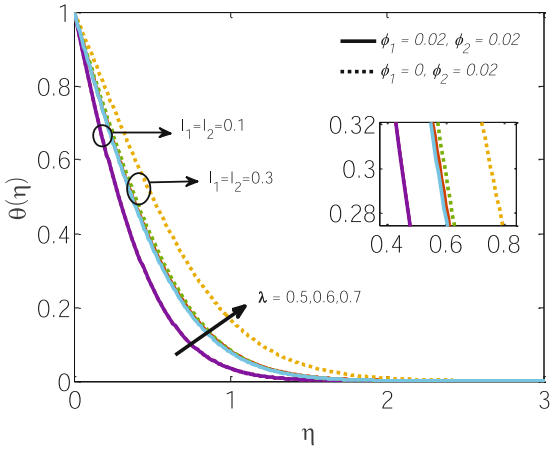


**Figure 11:** Temperature profile for different $\lambda$ with a comparison of NF and HNF with the impact of interfacial nanolayer thickness.

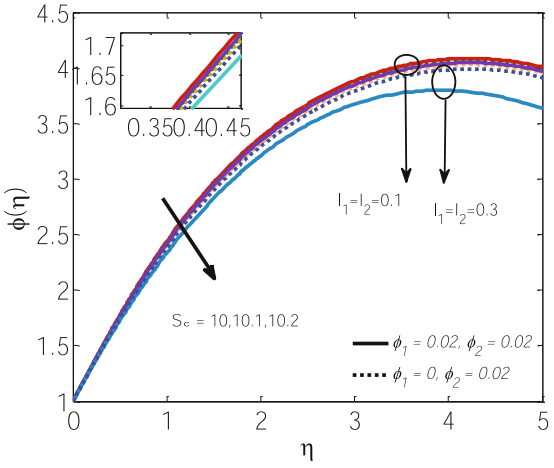


**Figure 13:** Concentration profile for different Sc with a comparison of NF and HNF with the impact of interfacial nanolayer thickness.

porosity variable $\lambda$ on the temperature profile is observed in Figure 11, which improves the temperature of the system with higher $\lambda$. The fluid finds more room in the system with better values of $\lambda$, which boosts the temperature and increases the thermal boundary layer thickness. It further implies that higher values of $\lambda$ (within the range of $0 \le \lambda \le 1$) significantly enhances the temperature profile. The molecules of the liquid become more active and more rapid due to the presence of $K_p$, which enriches the temperature at the surface and within boundary layer. Figure 12 shows the variation in the non-uniform inertia coefficient Fr on the temperature distribution. The consequence of the inertia increased with an increase in the non-uniform flow, which supports an improvement in the temperature profile. Hence, with a rise in the values of Fr, thermal boundary layer thickness increases.

## 4.3 Concentration profile

The result of the Schmidt number Sc on the concentration profiles is displayed in Figure 13. It is observed that a higher value of Schmidt number restricts the concentration profile. Physically, Sc represents the ratio of momentum diffusivity ($\nu_f$) to mass diffusivity ($D_B$). With an increase in Sc, it reduces the mass diffusivity $D_B$ and simultaneously reduces the solute boundary layer thickness. A comparison of the NFs and HNFs is observed in all the graphs with the thickness of the interfacial nanolayer of the NPs. It is observed that the concertation of the solute was higher for the HNF than the nanofluid, while the difference was not that significant. However, an increase in the thickness of the interfacial nanolayer of the NPs restricts the solute concentration and controls the solute boundary layer thickness. Figure 14

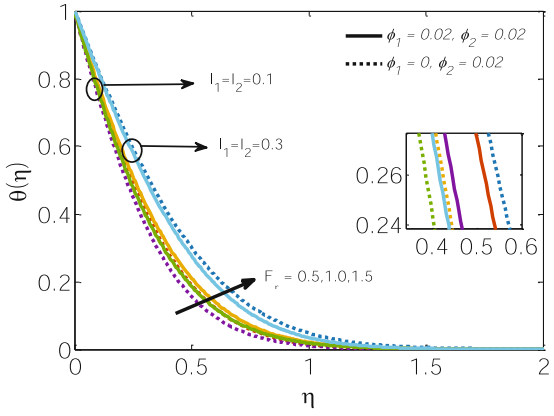


**Figure 12:** Temperature profile for different Fr with a comparison of NF and HNF with the impact of interfacial nanolayer thickness.

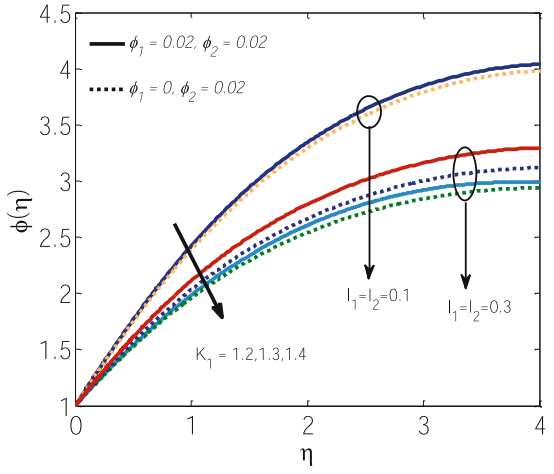


**Figure 14:** Concentration profile for different $K_1$ with a comparison of NF and HNF with the impact of interfacial nanolayer thickness.

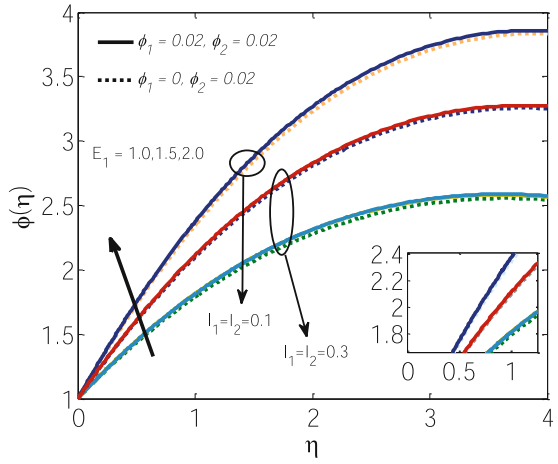


**Figure 15:** Concentration profile for different $E_1$ with a comparison of NF and HNF with the impact of interfacial nanolayer thickness.

demonstrates that the advanced outcomes of the chemical reaction parameter $K_1$ restrict the concentration profile close to the boundary layer and suppress the concentration boundary layer thickness. With advanced values of activation energy $E_1$, the concentration profile inclines, which supports the solutal boundary layer thickness (Figure 15).

## 4.4 Skin friction and Nusselt number profile

Figure 16 demonstrates the skin friction profile ($C_{fr}$) for $M$ and $\lambda$. The skin friction profile improves with higher values of $M$, while it shows an opposite feature with higher $\lambda$. It is due to that the magnetic parameter produces Lorentz force which enhanced the internal friction between the fluid molecules which significantly support the skin friction. Porosity parameters oppose the enhancement of the skin friction at the surface while the variation is not

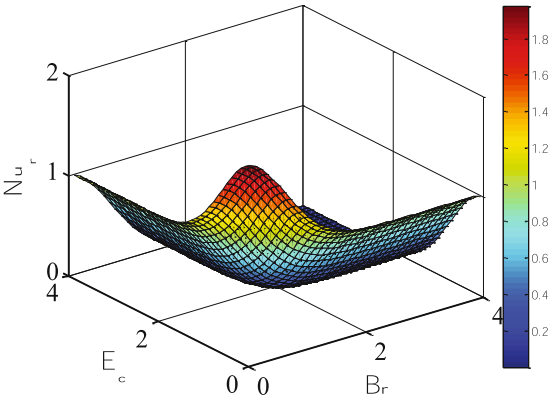


**Figure 17:** Nusselt number profile varies with Br and Ec.

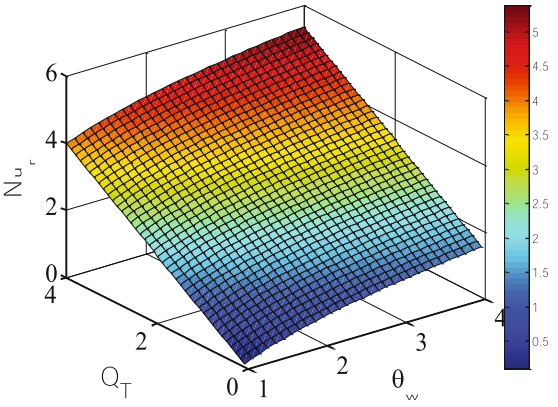


**Figure 18:** Nusselt number profile varies with $\theta$w and $Q$T.

highly significant as the magnetic parameters. Figure 17 demonstrates the Nusselt number $Nu_r$ profile that varies with Ec and Br. Eckert number Ec increases the temperature of the system due to the introduction of the viscous dissipation and thus reduces the heat transport rate. A

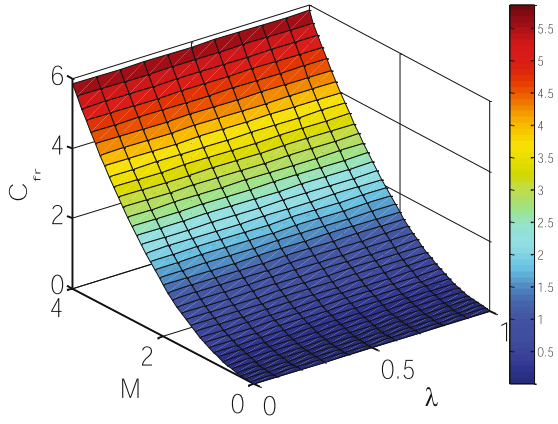


**Figure 16:** Skin friction profile varies with $M$ and λ.

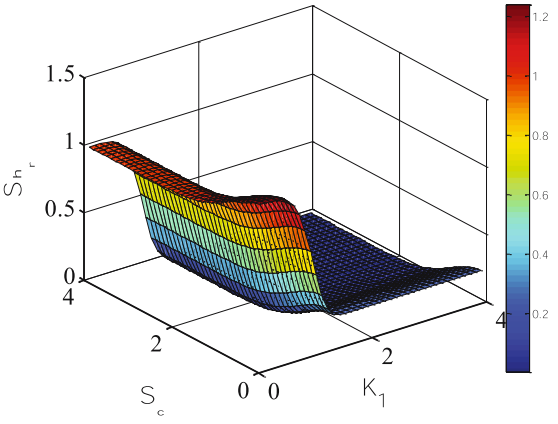


**Figure 19:** Sherwood number profile varies with Sc and $K_1$.

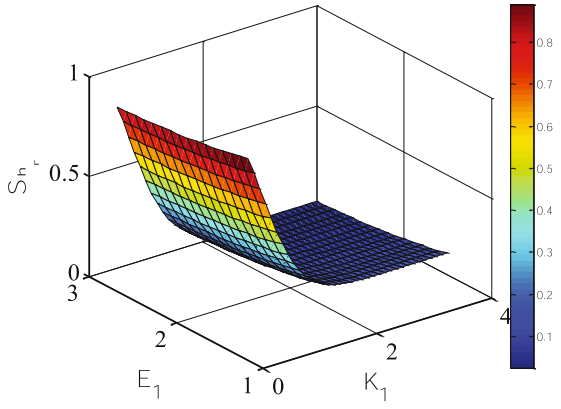


**Figure 20:** Sherwood number profile varies with *K*1 and *E*1.

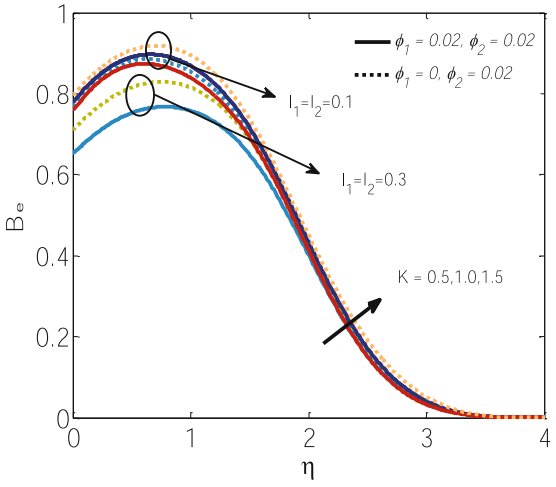


**Figure 23:** Bejan number for different *K* with a comparison of NF and HNF with the impact of interfacial nanolayer thickness.

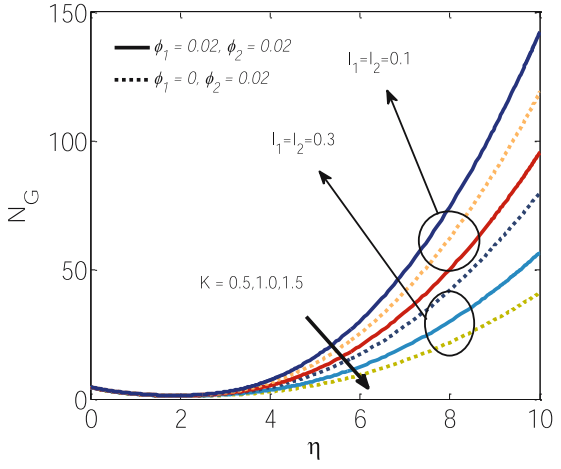


**Figure 21:** Entropy for different *K* with a comparison of NF and HNF with the impact of interfacial nanolayer thickness.

comparable trend is observed for the Brinkman number, which reduces the heat transfer rate due to the introduction of Joule heating. Impact of $Q_T$ and $\theta_w$ on the local Nusselt number $Nu_r$ is demonstrated in Figure 18. Parameters for heat generation and the local Nusselt number are increased by $Q_T$, and this is verified by the temperature ratio $\theta_w$. Figure 19 illustrates the Sherwood number profile that varies with Sc and $K_1$. With the increasing values of *Sc* and $K_1$, the Sherwood number profile is augmented. The Sherwood number profile is enhanced by the rising values of Sc and $K_1$ because an increase in the chemical reaction parameter increases the fluid particles' internal conductive resistance. Figure 20 illustrates the Sherwood number profile that varies with $E_1$ and $K_1$. With the increasing values of $E_1$ and $K_1$, the Sherwood number profile is declined. The internal

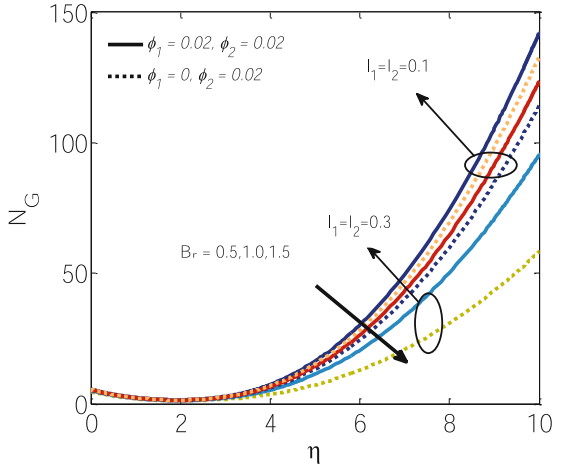


**Figure 22:** Entropy for different Br with a comparison of NF and HNF with the impact of interfacial nanolayer thickness.

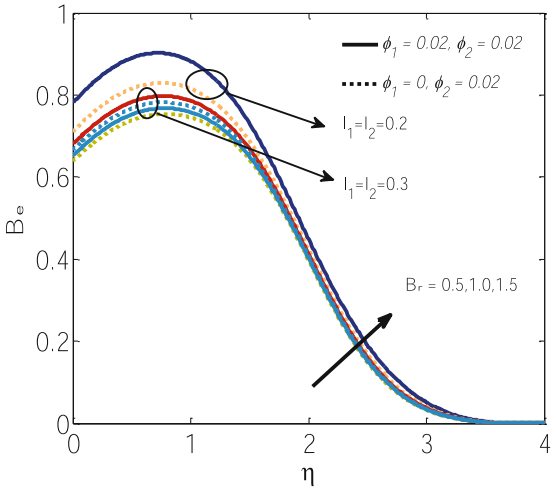


**Figure 24:** Bejan number for different Br with a comparison of NF and HNF with the impact of interfacial nanolayer thickness.

**Table 2:** Comparison values of $f'(0)$ for different values of Fr with Manzoor *et al*. [3] for $\phi_1 = \phi_2 = \lambda = M = 0$

| | **Fr = 0.5** | **Fr = 1.0** | **Fr = 1.5** |
|---|---|---|---|
| Manzoor *et al*. [3] | 0.241051 | 0.346591 | 0.462376 |
| Present | 0.241055 | 0.346594 | 0.462378 |

**Table 3:** Comparison of heat transfer rate $-\theta'(0)$ with Manzoor *et al*. [3] for $\phi_1 = \phi_2 = E_c = Q_T = \mathrm{Pr} = 0$

| **Rd** | **Manzoor *et al*. [3]** | **Present result** |
|---|---|---|
| 0.2 | 0.1968238 | 0.1968348 |
| 0.4 | 0.2401226 | 0.2401312 |
| 0.6 | 0.3365645 | 0.3365857 |

conductive resistance between the fluid particles is disrupted by the increase in activation energy, which causes the Sherwood number profile to decrease as $E_1$ and $K_1$ values rise.

### 4.5 Entropy generation

Figure 21 shows that entropy declines with higher values of the permeability parameter $K$. Entropy helps to observe the irreversibility of the system, which also deals with the heat loss of the system. With higher permeability, the intermolecular force between NPs gets slower. This nature is supported by the reduction in entropy. A comparison of the NF and HNF with the thickness of the nanolayers on the entropy and Bejan number has been displayed in each graph. The entropy was observed higher for the HNF than the NF. It is due to the presence of dual NPs, which generate more entropy in the system than mono NPs. A rise in the thickness of the interfacial nanolayer of the NP restricts the entropy of the system. A similar effect has been found for the Brinkman number (Figure 22). The Bejan number is inversely related to the total entropy of the system, and hence, an inverse trend is observed for the Bejan number (Figures 23 and 24).

## 5 Validation

Our results related with that of Manzoor *et al*. [3] for $f'(0)$ and $-\theta'(0)$ with certain conditions as noted in Tables 2 and 3, respectively. Their results show phenomenal promise, and this gives us confidence in our numerical method and conclusions.

## 6 Conclusion

In the current study, the thermal Marangoni convection flows in a steady Darcy-Forchheimer flow of nanomaterials are investigated with the effects of interfacial nanolayers. The entropy and Bejan number were also evaluated to display the system's irreversibility. It has been utilised to resolve the leading equations using the finite element method. Each graph shows the impact of the ratio of $I_1$ and $I_2$ nanolayers on temperature and velocity for various parameters. The tables also display the outcome of several parameters that fluctuate with HNF and NF that depend upon the outcomes of skin friction and heat transfer with the impact of the ratio of the nanolayers. A comparison was made with the ratio of nanolayers $I_1, I_2$, and between HNFs and NFs in each graph. Some of the major outcomes are as follows:

- Velocity profiles increase with Rd, $\lambda$ and decrease with $r^*$, $Q_T$, $M$, Fr.
- The temperature profiles increase with Rd, $M$, $Q_T$, Ec, $\lambda$, Fr.
- The concentration profiles increase with $E_1$ and decrease with Sc, $K_1$.
- The study of skin friction analysis improves with higher outcomes of $M$ and $\lambda$.
- The heat transfer rate increases with better outcomes of $\theta_w$ and $Q_T$, while decrease with better outcomes of Br and Ec.
- Physically heat is created by thermal radiation within the liquid, which enhanced the heat transfer rate.
- The mass transfer lessened with higher outcomes of $K_1$, $E_1$, and Sc.

This study can be helpful to understand the impact of the interfacial nanolayer on Marangoni bio-HNF flow over a rotating disk. In the future, we may extend this research by applying the heat transfer properties of ternary HNFs by applying three different types of NPs in the base fluid over any geometry, as this has potential industrial applications. Outcomes of the present study will be very helpful in several industries, including biosensors, nano- and microelectronics, atomic reactors, and medical tools, where Marangoni convection plays an important role in the presence of bio-HNF and further processing thermal control with the interfacial nanolayer thickness of the NPs.

**Acknowledgments:** Researchers Supporting Project number (RSPD2023R576), King Saud University, Riyadh, Saudi Arabia.

**Funding information:** This work was supported by Researchers Supporting Project number (RSPD2023R576), King Saud University, Riyadh, Saudi Arabia.

**Author contributions:** The authors equally conceived of the study, participated in its design and coordination, drafted the manuscript, participated in the sequence alignment, and read and approved the final manuscript. All authors have read and agreed to the published version of the manuscript.

**Conflict of interest:** The authors state no conflict of interest.

# References


[1] Ullah I. Heat transfer enhancement in Marangoni convection and nonlinear radiative flow of gasoline oil conveying Boehmite alumina and aluminum alloy nanoparticles. Int Comm Heat Mass Trans. 2022;132:105920.

[2] Khan MI, Qayyum S, Shah F, Kumar RN, Gowda RP, Prasannakumara BC, et al. Marangoni convective flow of hybrid nanofluid (MnZnFe2O4-NiZnFe2O4-H2O) with Darcy-Forchheimer medium. Ain Shams Eng J. 2021;12(4):3931–8.

[3] Manzoor U, Muhammad T, Farooq U, Waqas H. Investigation of thermal stratification and nonlinier thermal radiation in Darcy-Forchheimer transport of hybrid nanofluid by rotating disk with Marangoni convection. Int J Ambient Energy. 2022;43:6724–31.

[4] Mahanthesh B, Gireesha BJ, Shashikumar NS, Shehzad SA. Marangoni convective MHD flow of SWCNT and MWCNT nano liquids due to a disk with solar radiation and irregular heat source. Physica E. 2017;94:25–30.

[5] Hayat T, Khan MI, Farooq M, Alsaedi A, Yasmeen T. Impact of Marangoni convection in the flow of carbon–water nanofluid with thermal radiation. Int J Heat Mass Trans. 2017;106:810–5.

[6] Lin Y, Li B, Zheng L, Chen G. Particle shape and radiation effects on Marangoni boundary layer flow and heat transfer of copper-water nanofluid driven by an exponential temperature. Powder Technol 2016;301:379–86.

[7] Zhang J, Sekimoto A, Okano Y, Dost S. Numerical simulation of thermal-solutal Marangoni convection in a shallow rectangular cavity with mutually perpendicular temperature and concentration gradients. Phys Fluids. 2020;32:102108.

[8] Sheikholeslami M, Chamkha AJ. Influence of Lorentz forces on nanofluid forced convection considering Marangoni convection. J Mol Liq. 2017;225:750–7.

[9] Shaw S, Mahanta G, Das M. Thermal and solutal Marangoni stagnation point Casson fluid flow over a stretching sheet in the presence of radiation, Soret and Dufour effect with chemical reaction. Heat Trans Asian Res. 2019;48:323–42.

[10] Mahanta G, Das M, Shaw S, Mahala BK. MHD double-diffusive thermosolutal Marangoni convection non-Newtonian Casson fluid flow over a permeable stretchable sheet. Heat Trans. 2020;49:1788–807.

[11] Mousavi SB, Heris SZ. Experimental investigation of ZnO nanoparticles effects on thermophysical and tribological properties of diesel oil. Int J Hydrogen Ener. 2020;45:23603–14.

[12] Makinde OD, Aziz A. Boundary layer flow of a nanofluid past a stretching sheet with a convective boundary condition. Int J Ther Sci. 2011;50:1326–32.

[13] Ramya D, Raju RS, Rao JA, Chamkha AJ. Effects of velocity and thermal wall slip on magnetohydrodynamics (MHD) boundary layer viscous flow and heat transfer of a nanofluid over a non-linearly-stretching sheet: a numerical study. Prop Power Res. 2018;7:182–95.

[14] Choudhury R, Das SK. Visco-elastic MHD free convective flow through porous media in presence of radiation and chemical reaction with heat and mass transfer. J Appl Fluid Mech. 2014;7:603–9.

[15] Abdulrahman A, Gamaoun F, Kumar RV, Khan U, Gill HS, Nagaraja KV, et al. Study of thermal variation in a longitudinal exponential porous fin wetted with TiO2− SiO2/hexanol hybrid nanofluid using hybrid residual power series method. Case Stud Ther Eng. 2023;43:102777.

[16] Yan SR, Kalbasi R, Nguyen Q, Karimipour A. Rheological behaviour of hybrid MWCNTs-TiO2/EG nanofluid: a comprehensive modelling and experimental study. J Mol Liq. 2020;308:113058.

[17] Varun Kumar RS, Alhadhrami A, Punith Gowda RJ, Naveen Kumar R, Prasannakumara BC. Exploration of Arrhenius activation energy on hybrid nanofluid flow over a curved stretchable surface. ZAMM. 2021;101(12):e202100035.

[18] Mahanta G, Mohanta S, Mohanty D. Stability and convergence analysis of casson-nano fluid flow is heated non-linearly with viscous dissipation with convective boundary conditions. Int J Appl Eng Res. 2022;17:290–8.

[19] Xiong Q, Bozorg MV, Doranehgard MH, Hong K, Lorenzini GA. CFD investigation of the effect of non-Newtonian behaviour of Cu–water nanofluids on their heat transfer and flow friction characteristics. J Ther Anal Calo. 2020;139:2601–21.

[20] Abbas F, Ali HM, Shah TR, Babar H, Janjua MM, Sajjad U, et al. Nanofluid: Potential evaluation in automotive radiator. J Mol Liq. 2020;297:112014.

[21] Babar H, Ali HM. Towards hybrid nanofluids: preparation, thermophysical properties, applications, and challenges. J Mol Liq. 2019;281:598–633.

[22] Ghalambaz M, Roşca NC, Roşca AV, Pop I. Mixed convection and stability analysis of stagnation-point boundary layer flow and heat transfer of hybrid nanofluids over a vertical plate. Int J Numer Methods Heat Fluid Flow. 2019;30:3737–54.

[23] Kumar V, Madhukesh JK, Jyothi AM, Prasannakumara BC, Khan MI, Chu YM. Analysis of single and multi-wall carbon nanotubes (SWCNT/MWCNT) in the flow of Maxwell nanofluid with the impact of magnetic dipole. Comp TheorChem. 2021;1200:113223.

[24] Madhukesh JK, Prasannakumara BC, Kumar RSV, Rauf A, Shehzad SA. Flow of hydromagnetic micropolar-Casson nanofluid over porous disks influenced by Cattaneo-Christov theory and slip effects. J Porous Media. 2022;25(3):35–49.

[25] Javed MF, Khan MI, Khan NB, Muhammad R, Rehman MU, Khan SW, et al. Axisymmetric flow of Casson fluid by a swirling cylinder. Results Phys. 2018;9:1250–5.

[26] Ellahi R, Sait SM, Shehzad N, Ayaz Z. A hybrid investigation on numerical and analytical solutions of electro-magnetohydrodynamics flow of nanofluid through porous media with entropy generation. Int J Numer Meth Heat Fluid Flow. 2019;30(2):834–54.

[27] Dalir N, Dehsara M, Nourazar SS. Entropy analysis for magnetohydrodynamic flow and heat transfer of a Jeffrey nanofluid over a stretching sheet. Energy. 2015;79:351–62.

[28] Shah Z, Sheikholeslami M, Kumam P. Influence of nanoparticles inclusion into water on convective magnetohydrodynamic flow with heat transfer and entropy generation through permeable domain. Case Stud Ther Eng. 2020;21:100732.

[29] Raja MAZ, Tabassum R, El-Zahar ER, Shoaib M, Khan MI, Malik MY, et al. Intelligent computing through neural networks for entropy

generation in MHD third-grade nanofluid under chemical reaction and viscous dissipation. Waves Random Comp Media. 2022;32:1–25.
[30] Qasim M, Afridi MI. Effects of energy dissipation and variable thermal conductivity on entropy generation rate in mixed convection flow. J Thermal Sci Eng Appl. 2018;10:044501.
[31] Mahdavi M, Saffar-Avval M, Tiari S, Mansoori Z. Entropy generation and heat transfer numerical analysis in pipes partially filled with porous medium. Int J Heat Mass Trans. 2014;79:496–506.
[32] Khan MI, Khan TA, Qayyum S, Hayat T, Khan MI, Alsaedi A. Entropy generation optimization and activation energy in nonlinear mixed convection flow of a tangent hyperbolic nanofluid. Eur Phys J Plus. 2018;133:329.
[33] Khan MI, Ullah S, Hayat T, Waqas M, Khan MI, Alsaedi A. Salient aspects of entropy generation optimization in mixed convection nanomaterial flow Int. J Heat Mass Trans. 2018;126:1337–46.
[34] Jiang HF, Li H, Xu QH. Effective thermal conductivity of nanofluids considering interfacial nano-shells. Mater Chem Phys. 2014;148:195–200.
[35] Heyhat MM, Rajabpour A, Abbasi M, Arabha S. Importance of nanolayer formation in nanofluid properties: Equilibrium molecular dynamic simulations for Ag-water nanofluid. J Mol Liq. 2018;264:699–705.
[36] Mitiche I, Lamrous O, Makhlouf S. Effect of the interface layer vibration modes in enhancing thermal conductivity of nanofluids. Phys Rev E. 2019;100(4):042120.
[37] Chen JH, Han K, Wang S. Investigation of enhanced thermal properties of Cu Ar nanofluids by reverse non equilibrium molecular dynamics method. Powder Technol. 2019;356:559–65.
[38] Zeroual S, Loulijat H, Achehal E. Viscosity of Ar-Cu nanofluids by molecular dynamics simulations: effects of nanoparticle content, temperature and potential interaction. J Mol Liq. 2018;268:490–6.
[39] Yu W, Choi S. The Role of Interfacial Layers in the Enhanced Thermal Conductivity of Nanofluids: A Renovated Maxwell Model. J Nanoparticle Res. 2003;5:167–71.
[40] Henderson JR, Van Swol F. On the interface between a fluid and a planar wall. Mol Phys. 1984;51:991–1010.
[41] Khodayari A, Fasano M, Bigdeli MB, Mohammadnejad S, Chiavazzo E, Asinari P. Effect of interfacial thermal resistance and nanolayer on estimates of effective thermal conductivity of nanofluids. Case Stud Ther Eng. 2018;12:454–61.
[42] Li Y, Zhai Y, Ma M, Xuan Z, Wang H. Using molecular dynamics simulations to investigate the effect of the interfacial nanolayer structure on enhancing the viscosity and thermal conductivity of nanofluids. Int Comm Heat Mass Trans. 2021;122:105181.
[43] Gerardi C, Cory D, Buongiorno J, Hu LW, Mckrell T. Nuclear magnetic resonance-based study of ordered layering on the surface of alumina nanoparticles in water. Appl Phys Lett. 2009;95:253104.
[44] Hu C, Bai M, Lv J, Wang P, Zhang L, Li X. Molecular dynamics simulation of nanofluid's flow behaviors in the near-wall model and main flow model. Microfluid Nanofluid. 2014;17:581–9.
[45] Li L, Zhang Y, Ma H, Yang M. Molecular dynamics simulation of effect of liquid layering around the nanoparticle on the enhanced thermal conductivity of nanofluids. J Nanoparticle Res. 2010;12:811–21.
[46] Sarkar S, Selvam RP. Molecular dynamics simulation of effective thermal conductivity and study of enhanced thermal transport mechanism in nanofluids. J Appl Phys. 2007;102:074602.
[47] Fan W, Zhong F. Effects of Macroparameters on the Thickness of an Interfacial Nanolayer of $Al_2O_3$– and $TiO_2$–Water-Based Nanofluids. ACS Omega. 2020;5:27972–7.
[48] Gkountas AA, Benos LT, Sofiadis GN, Sarris IE. A printed-circuit heat exchanger consideration by exploiting an $Al_2O_3$-water nanofluid: Effect of the nanoparticles interfacial layer on heat transfer. Ther Sci Eng Prog. 2021;22:100818.
[49] Tillman P, Hill JM. Determination of nanolayer thickness for a nanofluid. Int Comm Heat Mass Trans. 2007;34:399–407.
[50] Kumar R, Sharma T, Vajravelu K. Melting heat transport in a mixed convective squeeze flow of a hybrid nanofluid with interfacial nanolayer effects. ZAMM. 2022;103(3):e202200092.
[51] Jiang H, Xu Q, Huang C, Shi L. The role of interfacial nanolayer in the enhanced thermal conductivity of carbon nanotube-based nanofluids. Appl Phys A. 2015;118:197–205.
[52] Zhao C, Cheung CF, Xu P. High-efficiency sub-microscale uncertainty measurement method using pattern recognition. ISA Trans. 2020;101:503–14. doi: 10.1016/j.isatra.2020.01.038.
[53] Li Z, Wang K, Li W, Yan S, Chen F, Peng S. Analysis of Surface Pressure Pulsation Characteristics of Centrifugal Pump Magnetic Liquid Sealing Film. Front Energy Res. 2022;10:937299. doi: 10.3389/fenrg.2022.937299.
[54] Gowda RP, Kumar RN, Khan U, Prasannakumara BC, Zaib A, Ishak A, et al. Dynamics of nanoparticle diameter and interfacial layer on flow of non-Newtonian (Jeffrey) nanofluid over a convective curved stretching sheet. Int J Modern Phys B. 2022;36(31):2250224.
[55] Chen W, Hou H, Zhang Y, Liu W, Zhao Y. Thermal and solute diffusion in α-Mg dendrite growth of Mg-5wt.%Zn alloy: A phase-field study. J Mater Res Technol. 2023;24:8401–13. doi: 10.1016/j.jmrt.2023.05.024.
[56] Yao H, Sun Z, Liang L, Yan X, Wang Y, Yang M, et al. Hybrid metasurface using graphene/graphitic carbon nitride heterojunctions for ultrasensitive terahertz biosensors with tunable energy band structure. Photon Res. 2023;11(5):858–68. doi: 10.1364/PRJ.482256.
[57] Khan MI, Waqas M, Hayat T, Khan MI, Alsaedi A. Chemically reactive flow of upper-convected Maxwell fluid with Cattaneo–Christov heat flux model. J Braz Soc Mech Sci Eng. 2017;39:4571–8.
[58] Luo Y, Liu J, Yang H, Liu H, Zeng G, Huang B. Enhanced Circular Dichroism by F-Type Chiral Metal Nanostructures. Photonics. 2023;10(9):1028. doi: 10.3390/photonics10091028.
[59] Zhao Q, Liu J, Yang H, Liu H, Zeng G, Huang B. High Birefringence D-Shaped Germanium-Doped Photonic Crystal Fiber Sensor. Micromachines. 2022;13(6):1–10. doi: 10.3390/mi13060826.
[60] Rehman F, Khan MI, Sadiq M, Malook A. MHD flow of carbon in micropolar nanofluid with convective heat transfer in the rotating frame. J Mol Liq. 2017;231:353–63.
[61] Chen J, Wen L, Bi C, Liu Z, Liu X, Yin L, et al. Multifractal analysis of temporal and spatial characteristics of earthquakes in Eurasian seismic belt. Open Geosci. 2023;15(1):20220482. doi: 10.1515/geo-2022-0482.
[62] Yin L, Wang L, Ge L, Tian J, Yin Z, Liu M, et al. Study on the thermospheric density distribution pattern during geomagnetic activity. Appl Sci. 2023;13(9):1–18. doi: 10.3390/app13095564.
[63] Schwartz L, Garboczi EJ, Bentz DP. Interfacial transport in porous media: Application to DC electrical conductivity of mortars. J Appl Phys. 1995;78(10):5898–908.
[64] Yin Z, Liu Z, Liu X, Zheng W, Yin L. Urban heat islands and their effects on thermal comfort in the US: New York and

New Jersey. Ecol Indic. 2023;154:110765. doi: 10.1016/j.ecolind.2023.110765.
[65] Yin L, Wang L, Li T, Lu S, Yin Z, Liu X, et al. U-Net-STN: A Novel End-to-End Lake Boundary Prediction Model. Land. 2023;12(8):1602. doi: 10.3390/land12081602.
[66] Leong KC, Yang C, Murshed SMS. A model for the thermal conductivity of nanofluids – effect of interfacial layer. J Nanoparticle Res. 2006;8:245–54.
[67] Xie HQ, Fujii M, Zhang X. Effect of interfacial nanolayer on the effective thermal conductivity of nanoparticle-fluid mixture. Int J Heat Mass Trans. 2005;48:2926–32.
[68] Mohanty D, Sethy N, Mahanta G, Shaw S. Impact of the interfacial nanolayer on Marangoni convective Darcy-Forchheimer hybrid nanofluid flow over an infinite porous disk with Cattaneo-Christov heat flux. Ther Sci Eng Prog. 2023;41:101854.